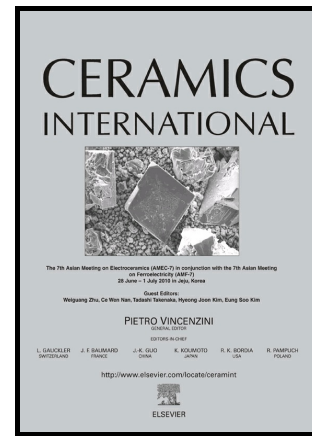


# Author's Accepted Manuscript

Retention of high dielectric constant sodium beta alumina via solution combustion: role of aluminum ions complexation with fuel

Bikesh Gupta, Pavan Pujar, Sib Sankar Mal, Dipti Gupta, Saumen Mandal



[www.elsevier.com/locate/ceri](http://www.elsevier.com/locate/ceri)

PII: S0272-8842(17)32250-2  
DOI: <https://doi.org/10.1016/j.ceramint.2017.10.061>  
Reference: CER116480

To appear in: *Ceramics International*

Received date: 16 June 2017  
Revised date: 29 September 2017  
Accepted date: 11 October 2017

Cite this article as: Bikesh Gupta, Pavan Pujar, Sib Sankar Mal, Dipti Gupta and Saumen Mandal, Retention of high dielectric constant sodium beta alumina via solution combustion: role of aluminum ions complexation with fuel, *Ceramics International*, <https://doi.org/10.1016/j.ceramint.2017.10.061>

This is a PDF file of an unedited manuscript that has been accepted for publication. As a service to our customers we are providing this early version of the manuscript. The manuscript will undergo copyediting, typesetting, and review of the resulting galley proof before it is published in its final citable form. Please note that during the production process errors may be discovered which could affect the content, and all legal disclaimers that apply to the journal pertain.

## Retention of high dielectric constant sodium beta alumina via solution combustion: role of aluminum ions complexation with fuel

Bikesh Gupta<sup>a</sup>, Pavan Pujar<sup>a,b</sup>, Sib Sankar Mal<sup>c</sup>, Dipti Gupta<sup>b</sup>, Saumen Mandal<sup>a\*</sup>

<sup>a</sup>*Department of Metallurgical and Materials Engineering, National Institute of Technology Karnataka (NITK) Surathkal, India.*

<sup>b</sup>*Plastic Electronics and Energy Laboratory, Department of Metallurgical Engineering and Materials Science, Indian Institute of Technology Bombay, Powai 400 076, India.*

<sup>c</sup>*Department of Chemistry, National Institute of Technology Karnataka (NITK) Surathkal, Mangalore, India.*

\*Corresponding author: [smandal@nitk.edu.in](mailto:smandal@nitk.edu.in),

### Abstract

In the present study, solution combustion technique has been explored to synthesize Sodium  $\beta$ -alumina (SBA;  $\text{NaAl}_{11}\text{O}_{17}$ ) powder and thin films. Three fuels namely urea, glycine and citric acid have been used to seek the feasibility of synthesizing crystalline SBA powder at low temperature. Also, the effect of nature of fuels used as well as calcination treatment on phase evolution and morphology of the as-combusted powder was investigated. Thermal analysis and X-ray diffraction studies suggest the formation of crystalline SBA powder at temperature as low as 259 °C, using urea in the combustion reaction whereas other fuels resulted in amorphous SBA phase and this variation in phase was found due to difference in exothermicity of the fuel used. Thermodynamic and spectroscopic analyses showed that the exothermicity of fuel depends on various factors like (i) standard heat of formation of fuel and (ii) the complexation offered by fuel to metal cations. Furthermore, sodium  $\beta$ -alumina thin film capacitor (metal-insulator-metal) was also fabricated using urea via spray combustion synthesis. The sodium  $\beta$ -alumina thin film showed a high dielectric value ( $\epsilon_r$ ) of ~21.

**Keywords:** Solution combustion,  $\beta$ - $\text{Al}_2\text{O}_3$ , Dielectric constant, Capacitor

## 1. Introduction:

Stoichiometric Sodium- $\beta$ -Alumina (SBA;  $\text{NaAl}_{11}\text{O}_{17}$ ) is a layered structure compound consisting of ‘conduction planes’, where mobile sodium ions ( $\text{Na}^+$ ) sandwiched between alternating spinel structured alumina ( $\text{Al}_2\text{O}_3$ ) blocks [1]. The  $\text{Na}^+$  ions are free to move in conduction planes [2], but their movement across (perpendicular to conduction plane) the spinel  $\text{Al}_2\text{O}_3$  blocks are restricted by inherent insulating nature of  $\text{Al}_2\text{O}_3$  blocks. Applying electric field to SBA film allows high degree of charge separation imparting high dielectric constant of SBA (~170 at 1 kHz) [3]. High dielectric constant along with high band gap (9 eV) [4] necessary to prevent gate leakage current when used as gate dielectric layer in thin film transistors (TFTs) makes SBA an eligible dielectric material to TFTs.

Various methods have been adopted to synthesize SBA powders like conventional solid state reaction [5], chemical co-precipitation [6], solution spray drying [7], solution spray freezing [8], vapor phase synthesis [9] etc. Due to overwhelming progress in thin film technologies, SBA films are also gaining huge interest because of its versatility as a thin film electrolyte in thin film batteries [10] as well as dielectric layer in thin film transistors [3, 11]. Some mostly used techniques for SBA thin film fabrication are electrophoretic deposition [10], laser chemical vapor deposition [12], tape casting [13], magnetron sputtering [14], sol-gel method [3] etc. Most of these synthesis techniques (both powder and thin film) are not cost effective; as they require high cost equipments as well as high temperature processing. Since SBA is a high temperature stable phase [15], high temperature processing is inevitable which limits its usage in various applications which needs low temperature processing.

Hence in quest of low temperature synthesis of SBA, solution combustion is a viable technique which compensate externally supplied heat by generating sufficient heat energy in situ [16]. Heat

energy generated due to combustion is utilized to synthesize desired materials, with much lower external heat input. Moderation of the heat generation during combustion is a key factor to control the evolution of desired phase. Solution combustion technique was extensively used to synthesize only powders, until Kim et al. in 2011 demonstrated that the same combustible precursors can be used to fabricate thin films [17]. Since then, these combustible precursors have been widely used by various thin film fabrication techniques like spin coating [18] and spray combustion synthesis (SCS) [19] to fabricate thin film devices. Unlike spin coating, SCS is advantageous to fabricate macroscopically continuous and dense film with desired thickness in a single step with improved property of devices with an added advantage of enabling large area device fabrication.

Several attempts have been made to synthesize SBA powders using solution combustion route. For instance, Mali et al. have synthesized SBA by calcining the combusted powder at 1400 °C, where citric acid was used as fuel [20]. However, most of the investigations have not been very efficient to synthesize single phase SBA powders at low temperature and does not provide detailed study of how different types fuels affects the phase evolution in SBA. Also, there are no reports on low temperature solution combustion derived crystalline SBA thin films as far as author is aware of.

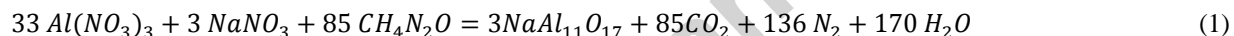
Hence, in the present study, solution combustion technique has been adopted to synthesize SBA powders as well as its thin film at low temperature. Three different fuels i.e. Urea, Glycine and Citric acid were used to investigate how these fuels alter the combustion reaction and to seek the feasibility of synthesizing SBA powder at low temperature. Subsequently, SCS was adopted to fabricate SBA thin films and its dielectric property was evaluated.

## 2. Experimental Section:

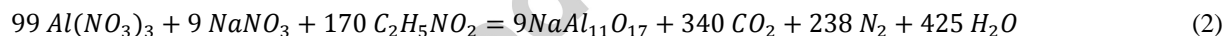
### 2.1 Powder synthesis:

Aluminum nitrate nonahydrate ( $\text{Al}(\text{NO}_3)_3 \cdot 9\text{H}_2\text{O}$ ; Molychem India (98% purity)) and Sodium nitrate ( $\text{NaNO}_3$ ; Nice chemicals, India (98% purity)) were the sources of Aluminum (Al) and Sodium (Na) respectively to synthesize SBA (Na:Al =1:11). Urea ( $\text{CH}_4\text{N}_2\text{O}$ ; SRL Pvt. Ltd India (99% purity)), Glycine ( $\text{C}_2\text{H}_5\text{NO}_2$ ; RFCL Limited India (99% purity)) and Citric acid ( $\text{C}_6\text{H}_8\text{O}_7$ ; Nice chemicals India (99.5% purity)) were selected as fuel. Stoichiometric amount of all precursors were taken as per the balanced chemical equations (Equation. 1-3).

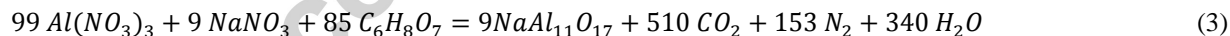
Urea as fuel ( $\text{F}_1$ )



Glycine as fuel ( $\text{F}_2$ )



Citric acid as fuel ( $\text{F}_3$ )



Solution of aluminum nitrate and sodium nitrate is prepared by dissolving stoichiometric amount of these two salts in 10 ml of Deionized (DI) water. Using water is advantageous over organic solvents namely 2-methoxy ethanol (2-ME), as aqueous solvent offers less combustion temperature compared to organic solvents [21]. Precursor solution of each fuel is prepared by dissolving the respective fuel in 10 ml of DI water solution. The combustible precursor solution using urea, glycine and citric acid will be referred as  $\text{F}_1$ ,  $\text{F}_2$  and  $\text{F}_3$  respectively hereafter. After stirring for 30 minutes, homogenized precursor solutions were heated at 90 °C on hot plate

allowing evaporation of solvent and forming viscous gel. Afterwards the hot plate temperature was raised to 300 °C to auto ignite the gel and resulted in the combustion with evolution of huge amount of gases and formation of voluminous, fluffy powder. Subsequently, the powders were crushed using mortar and pestle to obtain fine structure and calcined at different temperatures ranging from 600 °C to 900 °C at an interval of 100 °C for 2h of soaking time.

## 2.2 Capacitor fabrication:

The precursor employed for powder synthesis is further adopted for spray combustion to fabricate thin film. Prior to spray coating, the solvent cleaned indium tin oxide (ITO, Luminescence technology corps, 50 × 50 × 1.1 mm; 15 Ω) coated glass is preheated at a temperature of 300 °C. A nitrogen gas assisted sprayer (AB-15, nozzle diameter 0.3 mm) is loaded with precursor and held at a distance of 15 – 20 cm from the ITO substrate and sprayed the solution for 20 s repeatedly four times. The film fabricated at 300 °C was further annealed in furnace at 600 °C for 2 h. Here, ITO is acting as a bottom electrode; in order to complete the fabrication of thin film capacitor, 0.3 × 0.3 cm<sup>2</sup> pad of gold was then thermally evaporated on to SBA film, which serves as top contact electrode.

## 2.3 Characterization tools:

To understand the thermal behavior of the dried gels (obtained by subjecting the solutions in hot air oven at 80 °C for 24h), they were subjected to Thermogravimetric analysis (TGA; PerkinElmer, Thermo-gravimetric Analyzer TGA 4000) and Differential scanning calorimetry (DSC; NETZSCH DSC 404 F1) at heating rate of 10 °C/min in N<sub>2</sub> atmosphere (30 ml/min). To measure the Al<sup>3+</sup> ions concentration in each solutions, Inductively coupled plasma-Optical emission spectroscopy (ICP-OES; Thermo Fisher Scientific iCAP 7200) was carried out. Phase

analysis and crystallite size calculation were performed using X-ray diffraction (XRD; RIGAKU Miniflex 600) pattern recorded using Cu-K $\alpha$  radiation at scanning rate of 2 °/min. Instrumental broadening was removed using standard silicon powder. Scanning electron micrographs were recorded to study the powder morphology from Scanning Electron Microscope (SEM; JEOL model JSM 6380 system) with an energy-dispersive X-ray spectroscopy (EDS) attachment at an accelerating voltage of 20 kV. Morphology of the particles were observed using Transmission Electron microscopy (TEM; JEOL JEM-2010, Japan) operated at 100 kV. Phase analysis of thin film SBA was carried out using Glazing Incidence angle X-ray diffractometer (GIXRD; Philips PW 3040/60) at an incidence angle of 0.1 degrees using Cu-K $\alpha$  radiation at scanning rate of 2 °/min. X-ray photoelectron spectroscopy (XPS; PHI5000VersaProbeII) was performed on SBA thin film to determine the composition and chemical state of elements present in SBA film using Al K $\alpha$  radiation (~1486.6 eV). Deconvolution of Oxygen 1s spectra was done using Gaussian-Lorentzian peak function after Shirley background subtraction. The thickness of the film was measured by using profilometer (Ambios XP-2 Profilometer, SN 167). Capacitance measurement was performed using CVU module of a Keithley 4200-SCS and Novocontrol in ambient.

### **3. Results and Discussion:**

#### **3.1 TGA/ DSC analysis:**

Thermal analysis is one of the appropriate way to understand the combustion pathways in the system, especially combustion parameters like combustion temperature ( $T_c$ ; temperature at which auto ignition starts) and the amount of heat evolved during combustion reaction. Combustion reaction is marked by sudden weight loss and accompanied by evolution of heat energy at same temperature. The TGA thermograms and its 1<sup>st</sup> derivatives of the dried gel of each fuel is shown

in Fig. 1(a-c). As it can be observed from the TGA thermograms, mass loss in  $F_1$  happens in a single step, whereas in  $F_2$  and  $F_3$  mass loss occurs in a multi-step. There is continuous weight loss in all the systems up to 100 °C, which is due to solvent evaporation, followed by a sudden weight loss of approximately 75% at 257 °C, 60% at 190 °C and 43% at 167 °C in  $F_1$ ,  $F_2$  and  $F_3$  respectively. The sudden weight loss is accounted for by the escape of a huge amount of product gases evolved due to combustion (Table 1). Further, there is no weight loss observed in  $F_1$  beyond 257 °C, suggesting the combustion reaction is completed with the complete burning of the fuel, which could be further ascertained by the white color of the as-combusted powder (inset in Fig. 1(a)).

But in  $F_2$ , there was a continuous weight loss of approximately 9% up to 600 °C, which reveals that the combustion reaction is not sufficient to remove carbonaceous residue and a higher temperature is required to remove all the residue. The presence of carbonaceous residue could also be confirmed from the black color of the as-combusted powder, which later changes to white color when calcined at 600 °C for 2h (inset in Fig. 1(b)).

The multistep weight loss in  $F_3$  suggests the formation of some intermediate compound after the combustion reaction. This intermediate product is namely aconitic acid or citraconic acid, which is formed as a pyrolytic product of citric acid, inferred from the brown color appearance of the as-combusted powder (inset in Fig. 1(c)) [22]. The aconitic acid or citraconic acid decomposes with a weight loss of approximately 18% up to 400 °C as depicted from the TGA curve (Fig. 1(c)). This was further confirmed from the change in color of the as-combusted powder from brown to black when the as-combusted powder was heated at 400 °C for 2h (inset in Fig. 1(c)). Further, a weight loss of 15% was recorded up to 600 °C, which was mainly due to the burning of carbonaceous residue to  $\text{CO}_2$  and going off the system. The TGA analysis of all the gels suggests that, in the case of  $F_1$ , the as-

combusted powder is free from carbon residues (white powder) and no further calcination is required to obtain pure SBA powder.

To aid the further interpretation of the combustion processes of F<sub>1</sub>, F<sub>2</sub> and F<sub>3</sub> systems, TGA was supplemented by DSC analysis. The DSC thermograms of F<sub>1</sub>, F<sub>2</sub> and F<sub>3</sub> are shown in Fig. 2(a-c). Broad endothermic peaks around 92 °C, 110 °C and 110 °C in Fig. 2(a-c), is attributed to solvent evaporation. Additionally, two endothermic peaks are also observed around 147 °C and 470 °C in Fig. 2(c) which is due to the removal of bound water and carbonaceous residue respectively. Sharp exothermic peaks at 259 °C, 189 °C and 169 °C as observed in Fig. 2(a-c), are due to the redox reaction between fuel metal complex and nitrate releasing huge amount of heat energy [16]. These exothermic peaks in DSC and the sudden weight loss in TGA are concurrent at same temperature suggesting the combustion temperature (T<sub>c</sub>) to be 259 °C, 189 °C and 169 °C in F<sub>1</sub>, F<sub>2</sub> and F<sub>3</sub> respectively. The enthalpy of combustion reaction ( $\Delta H$ ) or in other words the amount of heat energy released during combustion reaction calculated using DSC is tabulated in Table 1. The difference in exothermicity as observed in F<sub>1</sub>, F<sub>2</sub> and F<sub>3</sub> could be explained by considering the factors like (i) standard heat of formation of each fuel ( $\Delta H_f^\circ$ ) and (ii) complex formation capability of fuels with metal ions.

The amount of heat released during combustion reaction or the heat of the reaction can be calculated theoretically from the equation mentioned below [23].

$$Q = \Delta H = \Delta H_f^\circ(\text{products}) - \Delta H_f^\circ(\text{reactants}) \quad (4)$$

Where Q or  $\Delta H$  is the heat of the reaction (enthalpy of the combustion reaction),  $\Delta H_f^\circ$  is the standard heat of formation of each component.

$$\Delta H_f^\circ(\text{products}) = \Delta H_f^\circ(\text{NaAl}_{11}\text{O}_{17}) + \Delta H_f^\circ(\text{H}_2\text{O}) + \Delta H_f^\circ(\text{CO}_2) + \Delta H_f^\circ(\text{N}_2) \quad (5)$$

$$\Delta H_f^\circ(\text{reactants}) = \Delta H_f^\circ(\text{Al}(\text{NO}_3)_3) + \Delta H_f^\circ(\text{NaNO}_3) + \Delta H_f^\circ(\text{fuel}) \quad (6)$$

From the above equations, it is evident that, the heat evolved during combustion reaction ( $\Delta H$ ) could be maximized by maximizing the difference in  $\Delta H_f^\circ$  of products and reactants. Since the products obtained in all the three cases of combustion reactions are theoretically same (Equation 1-3), it is easily understood that ( $\Delta H$ ) of combustion reaction is significantly affected by  $\Delta H_f^\circ$  of reactants and more precisely by  $\Delta H_f^\circ(\text{fuel})$  (Equation 6). Thus, ( $\Delta H$ ) of combustion reaction can be altered by selecting different types of fuels. Since, all the fuels used in the present study have negative  $\Delta H_f^\circ$  (see Table 1); increase in its negative value will certainly decrease the  $\Delta H$  value, evident from Equation (4). Since urea have the least negative  $\Delta H_f^\circ$  (-333.5 kJ/mole) and citric acid has the most negative  $\Delta H_f^\circ$  (-1543.8 kJ/mole) value, theoretically, the heat evolved during combustion will be least in F<sub>3</sub> and highest in F<sub>1</sub>. The same was also observed experimentally. The amount of heat evolved during combustion reaction (obtained from DSC) in F<sub>1</sub> reached highest value (1452.4 J/g) while it was least in F<sub>3</sub> (161.9 J/g).

However, there is significant difference in  $\Delta H$  of F<sub>1</sub> (1452.4 J/g) and F<sub>2</sub> (415.7 J/g), although there is not much difference in  $\Delta H_f^\circ$  of urea (-333.5 kJ/mole) and glycine (-528.5 kJ/mole). This could be accounted by yet another important factor; complexation of metal cations with different fuels. The heat energy evolved during combustion reaction is due to a redox reaction between the oxidizer (nitrate) and reducer (fuel). During the redox reaction, there is transfer of electrons between the two species and stored chemical energy is converted into heat energy. This suggest that intensity of redox reaction depends on number of electrons taking part in the redox reaction.

Complexation involves ligand and electrons in the chelation with metals which will reduce the effective number of electrons to take part in the redox reaction [24]. Consequently, the intensity of redox reaction (and thus the heat energy evolved due to redox reaction) between metal fuel complex and nitrates will drop down significantly, as there will be fewer number of electrons to take part in redox reaction due to complexation. Hence, more complexation may lead to reduction in the intensity of the combustion reaction.

Complexation of metal cations with fuel primarily depends upon the type of ligand groups present in the fuel. For instance, urea has only amine group at both ends, while glycine has amine group as well as carboxylic group at two ends to form complex with metal cations (Fig. S1). This will certainly create difference in the complexation capability of both the fuels. To study the extent of complexation of each fuel with  $\text{Al}^{3+}$  ions, ICP-OES was performed and results are shown in Fig. 2(d). As observed, the concentration of free  $\text{Al}^{3+}$  ions is least in  $\text{F}_2$  while compared to  $\text{F}_1$  and  $\text{F}_3$ , which indicates that glycine forms good complex with metal ions as compared to urea ( $\text{F}_1$ ) and citric acid ( $\text{F}_3$ ). This is due to presence of carboxylic group at one end and amino group at other end (Zwitterionic character) which equip glycine with a unique ability to form complex with metal ions of varying ionic sizes [25]. Since glycine forms good complex with metal cations compared to urea, it is obvious that  $\text{F}_2$  will have lesser evolution of heat energy during combustion as compared to  $\text{F}_1$ .

Furthermore, combustion temperature ( $T_c$ ) of the solution is also contingent upon the decomposition temperature ( $T_d$ ) of the fuel used in the reaction as demonstrated by Manukyan et al. [27]. This holds true in the present study too. The  $T_d$  of each fuel and  $T_c$  of the reaction is

tabulated in Table 1, and from a close inspection, we can infer that the  $T_c$  is certainly affected by the  $T_d$  of fuel. For instance, urea starts to decompose at 250 °C and the combustion in  $F_1$  is observed at 259 °C (Table 1), which are close by temperatures. Similarly, from the experimental studies it is observed that  $T_c$  of  $F_2$  and  $F_3$  is at 189 °C and 169 °C respectively, while the decomposition temperature of glycine and citric acid starts at 180 °C and 165 °C respectively (Table1), which also represent that combustion temperature ( $T_c$ ) of the solution and decomposition temperature ( $T_d$ ) of the fuel does not have much variation. Since the two temperatures are nearby, it reveals that indeed  $T_d$  is an influential factor for determining  $T_c$ . So while selecting a fuel, its decomposition temperature should also be taken care of, in order to synthesize any material at low temperature by combustion route.

Hence, from the above thermal analysis it can be summarized that, fuel plays an important role in combustion synthesis, as selection of fuel helps in tuning the exothermicity as well the combustion temperature of the reaction.

### 3.2 XRD analysis of SBA powder:

The XRD spectra of powders produced from  $F_1$  (urea based solution) is shown in Fig. 3(a). The XRD pattern of as-combusted powder as well as of powders calcined at different temperature suggest the formation of SBA phase and peaks are in well agreement with JCPDS card number 32-1033. Since SBA crystallizes in hexagonal crystal structure [29], lattice parameter is calculated using Equation (7) and values are tabulated in Table S1 (supplementary information).

$$\frac{1}{d^2} = \frac{4}{3} \left( \frac{h^2 + hk + k^2}{a^2} \right) + \left( \frac{l^2}{c^2} \right) \quad (7)$$

Where  $d$  is the distance between adjacent planes,  $(hkl)$  is the Miller indices,  $a$  and  $c$  are lattice parameters. The single peak around  $2\theta = 29^\circ$  of Bragg angle, in the as-combusted powder, correspond to unreacted Na (JCPDS card number 003-0598). The presence of Na may be due to very short time span of combustion reaction which may not be sufficient for all the Na atoms to diffuse into the SBA crystal structure. However, the Na peak disappears when the powder is calcined at  $600^\circ\text{C}$  for 2h, suggesting diffusion of Na into the SBA crystal structure. This is quite possible, as sufficient time is available for Na diffusion into the SBA crystal structure (2h of calcination at  $600^\circ\text{C}$  against very short time span of combustion reaction). This could primarily be confirmed by the lattice parameter change along  $c$ - axis in SBA crystal structure. As noted in the earlier studies, the deficiency of  $\text{Na}^+$  in the conduction plane of SBA crystal structure will cause lattice parameter reduction along  $c$ -axis due to the collapse of the Al-O-Al interconnecting bridge and layers move closer to each other along  $c$ - axis [30]. The lattice parameter along  $c$ -axis of as-combusted SBA powder is  $22.0541 \text{ \AA}$ , whereas of SBA powder calcined at  $600^\circ\text{C}$  is about  $22.5202 \text{ \AA}$  (see Table S1). The slight increase in the lattice parameter in the powder calcined at  $600^\circ\text{C}$  clearly suggests that Na has diffused into the SBA structure. The formation of SBA phase in as-combusted powder produced from  $F_1$  at extremely low temperature is attributed to the highly exothermic reaction observed in  $F_1$ . The crystalline SBA phase is retained and no further phase changes were observed upto  $900^\circ\text{C}$ .

The XRD pattern of powder produced from  $F_2$  (glycine based solution) is shown in Fig. 3(b). As-combusted powder shows a broad peak at around  $2\theta = 22^\circ$  of Bragg angle, which corresponds to formation of a secondary  $\text{Na}_5\text{AlO}_4$  phase (JCPDS card number 037-0208). The primary reason for this phase to form is low exothermicity of the combustion reaction in  $F_2$ , which may not be sufficient to form the desired SBA phase. Further, it can be seen that crystallization of a new

phase in the powder begins at 700 °C with simultaneous reduction in intensity of Na<sub>5</sub>AlO<sub>4</sub> peak. This new phase could be matched with mullite like alumina (m-Al<sub>2</sub>O<sub>3</sub>) phase (JCPDS card number 12-0539). This phase is reported to be stable from 700 °C to 1000 °C [31] and is regularly observed as an intermediate phase while synthesizing SBA, where processing technique involves molecular level mixing of precursors- solution combustion also falls in the same category [32]. Furthermore, a small quantity of SBA phase could have also formed at temperature above 800 °C, as some SBA peaks (low intensity) were also observed in Fig. 3(b).

The XRD pattern of powder produced from F<sub>3</sub> (citric acid based solution) is shown Fig. 3(c). The as-combusted powder seems to be amorphous in nature possibly due to low exothermicity of the combustion reaction. Further, when the same powder was calcined at higher temperature, transformation from amorphous to crystalline m-Al<sub>2</sub>O<sub>3</sub> phase was observed. As seen in Fig. 3(b) and 3(c), the XRD peaks became sharper with increase in the calcination temperature, indicating enhancement in the crystallinity of the powders.

Mullite like alumina (m-Al<sub>2</sub>O<sub>3</sub>) phase is reported to crystallize in two different crystal structures; tetragonal and orthorhombic. The presence of the respective phases can be distinguished from XRD spectra: a doublet in the XRD peak at  $2\theta = 26^\circ$  is a representative of an orthorhombic phase formation whereas a singlet at the same position accounts for tetragonal phase [33]. As seen from the inset of Fig. 3(b) and 3(c), the peak around  $2\theta = 26^\circ$  has single reflection, suggesting tetragonal phase formation of m-Al<sub>2</sub>O<sub>3</sub>. Thus, lattice parameter of m-Al<sub>2</sub>O<sub>3</sub> is calculated using Equation (8), as given below (used for tetragonal crystal structure) and the calculated lattice parameter values are tabulated in Table S1 (supplementary information).

$$\frac{1}{d^2} = \left( \frac{h^2 + k^2}{a^2} \right) + \left( \frac{l^2}{c^2} \right) \quad (8)$$

Where  $d$  is the distance between adjacent planes,  $(hkl)$  is the Miller indices,  $a$  and  $c$  are lattice parameters. The lattice parameter values calculated are around:  $a = 7.7592 \text{ \AA}$  and  $c = 2.92667 \text{ \AA}$  and are in well agreement with previous literature [34].

Moreover, an interesting phenomenon can be observed in XRD patterns of powders produced from  $F_2$  and  $F_3$  (Fig. 3(b) and 3(c)). The  $m\text{-Al}_2\text{O}_3$  phase crystallization starts predominantly at  $700 \text{ }^\circ\text{C}$ , in the powders produced from  $F_2$ , whereas the same is observed in  $F_3$  at  $800 \text{ }^\circ\text{C}$ . This difference in crystallization temperature of  $m\text{-Al}_2\text{O}_3$  phase may be attributed to different types of fuels used and their difference in complex formation ability with metal cations. Various researchers found that the crystallization temperature of SBA and their intermediate phases like  $m\text{-Al}_2\text{O}_3$  increases, as  $\text{Al}_2\text{O}_3$  content of the powder increases [35, 36]. Complexation of fuels with metal cations results in presence of cations in final product which in turn may vary the formation of  $\text{Al}_2\text{O}_3$  phase and its total quantity in the final product [37]. From the ICP-OES analysis (Fig. 2(d)) it can be observed that concentration of free  $\text{Al}^{3+}$  ion is less in  $F_2$  than  $F_3$ . So here, it can be said that concentration of free  $\text{Al}^{3+}$  ions may affect the in-situ formation of  $\text{Al}_2\text{O}_3$ ; lesser concentration of free  $\text{Al}^{3+}$  ion results in lesser amount of in situ  $\text{Al}_2\text{O}_3$  formation, which in turn curtails the crystallization temperature of  $m\text{-Al}_2\text{O}_3$  phase in powder produced from  $F_2$ .

The crystallite size of the various powders (as-combusted and calcined at different temperatures) is calculated using Debye Scherer formula (Equation 9-10).

$$t = \left( \frac{0.9\lambda}{\beta \cos\theta} \right) \quad (9)$$

$$\beta = \sqrt{\beta_{sample}^2 - \beta_{instrument}^2} \quad (10)$$

Where  $t$  is the crystallite size,  $\lambda$  is the wavelength of the radiation (1.54056 Å for CuK $_{\alpha}$  radiation),  $\theta$  is the peak position,  $\beta$  is the corrected FWHM obtained by subtracting the instrumental broadening ( $\beta_{\text{instrument}}$ ) from the as obtained FWHM from the powder ( $\beta_{\text{sample}}$ ) as shown in Equation (10). The crystallite size of powders obtained from F $_1$ , F $_2$  and F $_3$  as a function of temperature is shown in Fig. 3(d). Comparing the crystallite size of powders calcined at 800 °C (as all powders are well crystallized at this temperature), it is observed that powders obtained from F $_1$  has the highest crystallite size (56 nm), possibly due to highest exothermicity of F $_1$  solution, while compared to F $_2$  and F $_3$ . Moreover, it is also observed that, as calcination temperature increases, the crystallite size also increases, which is quite natural phenomena observed in calcination of powders. Hence from the phase analysis it is evident that fuel has an important role to play in obtaining crystalline SBA phase.

### 3.3 SEM analysis of SBA powder:

To study the morphology of the produced powders, they were subjected to SEM analysis as shown in Fig. (4-6). The SEM micrograph of powder (as-combusted) produced from F $_1$  is shown in Fig. 4(a) where layered structure could be observed which resembles with layered structure of SBA. Further, elemental analysis of this layered structure is done with energy dispersive spectroscopy (EDS) analysis (Fig. 4(c)), which shows that the atomic percent of Na:Al is approximately 1:11; similar to stoichiometric ratio of Na and Al in SBA (NaAl $_{11}$ O $_{17}$ ). In the same powder (as-combusted), growth of some rod like particles are also observed as shown in Fig. 4(b). The rod like morphology could be attributed to instantaneous high temperature reached during combustion reaction.

Plate like hexagonal particles could be observed in the powder (produced from F<sub>1</sub>), while calcined at 900 °C as shown in Fig. 4(d). Similar plate like hexagonal particle morphology was observed by Mali et al. in their work, while they calcined the as-combusted SBA powder at 1400 °C for 1 hour [20]. Presence of plate like hexagonal particles could be a confirmation of formation of SBA phase, as SBA has hexagonal crystal structure.

The SEM micrograph of powder (as-combusted) produced from F<sub>2</sub> is shown in Fig. 5 (a) where pores in the powder could be observed. During combustion reaction different types of gases like N<sub>2</sub>, CO<sub>2</sub>, H<sub>2</sub>O evolves, leaving behind pores in the powder (moles of gases evolved per mole of product formed is shown in Table 1). In addition to that, these gases also assist in dissipating the heat energy generated during combustion which prevents particle growth. The calculated mean pore size in the powder is around  $0.45 \pm 0.26 \mu\text{m}$ . Moreover, the powder calcined at 900 °C shows two different morphologies viz. (i) hexagonal particles and (ii) needle like particles, as shown in Fig. 5(b) and (c). Presence of hexagonal shaped particles could be attributed to presence of small trace of SBA (Fig. 5(b)) and needle like particle morphology could be attributed to the presence of m-Al<sub>2</sub>O<sub>3</sub> phase, which is in good agreement with the XRD analysis. It has been reported that m-Al<sub>2</sub>O<sub>3</sub> prefers to crystallize in needle like morphology or plate like morphology [20, 38, 39]. However, needle like morphology is reported to show improved mechanical properties and thermal shock resistance over plate like morphology [40].

Similarly, powder (as-combusted) produced from F<sub>3</sub> also contains pores as seen in Fig. 6(a). The calculated mean pore size is around  $1.37 \pm 0.84 \mu\text{m}$ , which is slightly higher than pore size in powder obtained from F<sub>2</sub> (see Table 1). This difference in pore size may be due to difference in heat energy generated during combustion reaction in each fuel. Higher heat energy evolved causes coalescence of the particles, which in turn may lead to pore size reduction. However, the

powder calcined at 900 °C resulted in two different morphologies viz. (i) needle like tubes along with (ii) tape like structures. Similar needle like tubes have been observed by Soares et al., when they attempted to synthesize  $m\text{-Al}_2\text{O}_3$  phase by decomposing topaz [41]. The phase evolution in XRD at different temperature and their corresponding morphology are in good agreement with each other. Hence, it can be summarized that the morphology of the produced powder by solution combustion route, depends on the type of fuels used (as different fuel offers different properties in terms of complexation, exothermicity, and gases evolved during combustion etc.).

### **3.4 TEM analysis of SBA powder:**

The TEM micrographs of powder produced from  $F_1$  is shown in Fig. 7(a-c). As-combusted powder shows agglomerated particles with irregular morphology (Fig. 7(a)). Moreover, some rod like particles are also observed in the as-combusted powder, as shown in Fig. 7(b). One particle with uniform diameter of around 52 nm is seen, whereas in case of the other two rod like particles, it is observed that, the diameter of the rods have increased slightly than the nose of the rods, and hence these particles look distorted rod like structure. This might be due to the high exothermic heat generated in  $F_1$ , caused sintering of the rod like particle with some other particles. The selected area electron diffraction (SAED) pattern (inset in Fig. 7(b)) confirms the presence of polycrystalline SBA. The interplanar spacing is measured from the high resolution lattice image, which is found to be 3.92 Å as shown in Fig. 7(c).

### **3.5 XRD analysis of SBA thin films:**

As inferred from the powder studies, among the three fuels used (i.e. urea, glycine, citric acid) crystalline SBA was obtained only from  $F_1$  in the as-combusted powder and thus  $F_1$  was used to prepare the thin films of SBA via spray combustion synthesis. The XRD of the fabricated thin

film using  $F_1$  at two different temperatures is shown in Fig. 8. As observed from Fig. 8, the film fabricated at 300 °C shows amorphous state of SBA with an intense peak of Na. The formation of amorphous SBA phase could be understood from the fact that, the higher exposed surface of film as compared to powders causes 'significant heat dissipation (which was generated during combustion reaction), leading to inefficient utilization of generated heat in the film for crystalline SBA phase formation. This result is quite different from XRD of the powder (as-combusted) using the same solution where we obtained crystalline SBA phase. Moreover, the presence of Na peak in the film, could be due to short span of time (as combustion happens very fast), which is not sufficient for diffusion of Na in to the  $\beta$ - $Al_2O_3$  lattice. However, when the film was heated at 600 °C for 2h, it started to crystallize and forms crystalline SBA phase along with disappearance of Na peak, which could be due to diffusion of Na atoms into the SBA lattice structure. Similar phenomena were also observed in the as-combusted powder obtained from  $F_1$  (Fig. 3 (a)). Obtaining a crystalline SBA film at such a low temperature could be due to the high amount of heat energy generated initially in the  $F_1$  system. Generally SBA film exhibits amorphous nature until heated at elevated temperature; for instance Zhang et al. reported solution processed crystalline SBA film at 1000 °C treated for 15h [42]. But, with the aid of heat generated during combustion reaction one can successfully obtain crystalline SBA film at 600 °C for 2h.

### 3.6 XPS analysis of SBA thin films:

To have a better understanding of the elemental composition in the SBA film, GIAXRD was supplemented by XPS analysis. Fig. S1 in the supplementary information shows the XPS survey scan of the SBA films fabricated at 300 °C and 600 °C using  $F_1$ . The XPS peaks centered around 73.6 eV, 1072 eV and 531 eV, as shown in Fig. S1, represents aluminum ( $Al2p$ ), sodium ( $Na1s$ )

and oxygen (O1s) binding energies respectively which confirms the presence of Al, Na and O atoms in both the SBA films.

Further, to investigate the different chemical states of oxygen atom in the films, O1s spectra was deconvoluted into three principal peaks centered at 530.6 eV, 531.7 eV and 532.6 eV, as seen in Fig. 9 (a) and (b). The peak area, FWHM and reduced  $\chi^2$  data can be found in Table S2 of the supplementary information. The 1<sup>st</sup> peak centered at 530.6 eV corresponds to M-O-M lattice species and reflects the metal oxide formation. The 2<sup>nd</sup> peak centered at 531.7 eV reflects the formation of bulk or surface metal hydroxide (M-OH) species. The 3<sup>rd</sup> peak centered at 532.6 eV is attributed to weakly bound (M-OR) species like H<sub>2</sub>O and CO<sub>2</sub> [43]. The presence of M-O-M lattice species is important to a dielectric material for improving dielectric constant and leakage current properties. However, the presence of hydroxyl species (M-OH) is detrimental to dielectric property, because it enhances the leakage current by providing a conduction path for electron flow in the dielectric materials [44]. So, higher percentage of M-O-M lattice formation is desired over the other species like M-OH and M-OR, though their (M-OH and M-OR) presence is always observed in solution processed metal oxides (MO<sub>x</sub>).

The concentration of each oxygen binding states (M-O-M, M-OH and M-OR) in SBA film can be calculated by taking ratio of each peak area to the total O1s peak area. As observed in Fig. 9(a), the SBA film fabricated at 300 °C shows higher percentage of M-O-M lattice species (about 47 %) than M-OH species (about 37%). Generally, at lower temperatures (<300 °C), it is observed that concentration of M-O-M will be less as compared to M-OH concentration, due to insufficient energy available for M-O-M lattice formation. But in present study, the concentration of M-O-M species is quite high compared to M-OH species. In addition to high heat energy generated during combustion reaction, lattice enthalpy of metal oxide ( $\Delta H_L$ ) could

also be crucial in M-O-M lattice formation [43]. Hennek et al. observed that metal cations whose  $\Delta H_L$  is more, compared to other metal cations, favors more M-O-M lattice formation [43]. Since  $Al^{3+}$  is also reported to have high  $\Delta H_L$ [43], we can assume that  $\Delta H_L$  factor is also playing a role in enhancing the M-O-M concentration in SBA film fabricated at 300 °C. Moreover, the film fabricated at 600 °C shows further increase in the M-O-M concentration (56 %) over other species, as seen in Fig. 9(b). This increase is obvious because higher processing temperature favors M-O-M formation.

Na1s and Al2p representative spectra of SBA thin film are shown in Fig. 9(c) and (d) respectively. As discerned from Fig. 9(c), the Na1s peak at 600 °C is slightly shifted towards higher binding energy state with respect to Na1s peak at 300 °C. This shift may be accounted for change in state of Na atoms in SBA film as observed in GIAXRD studies (Fig. 8). At 300 °C, presence of unreacted Na was observed (reason explained earlier), whereas at 600°C the Na atoms diffused into the SBA lattice (Fig. 8), which would have changed the ionic state of Na, that led to peak shift of Na. However, no such shift in binding energy of aluminum (Al2p) was observed in SBA films.

### 3.7 Capacitance measurement:

The schematic as well as the fabricated device is shown in Fig. 10. The capacitance response as a function of frequency and voltage is shown in Fig. 11. From Fig. 11(a), one can infer that the capacitance of the capacitor reduces as frequency increases, which is obvious as the polarization response time is limited by the ion mobilities in the dielectric layer [3]. The dielectric constant of SBA film is calculated from the equation given below.

$$C = \frac{\epsilon_0 \epsilon_r A}{d} \quad (11)$$

Where  $C$ ,  $\epsilon_0$ ,  $\epsilon_r$ ,  $A$  and  $d$  are the capacitance offered by the capacitor, permittivity of free space, relative permittivity of the dielectric material, effective area of dielectric layer between the two electrodes and the thickness of the dielectric layer respectively. The thickness of the film is around 800 nm as obtained from profilometer. The dielectric constant of SBA film calculated from the Equation (11) is around 21 at 1 kHz, which is 3 times higher than the solution processed pure Alumina ( $\text{Al}_2\text{O}_3$ ;  $\epsilon_r \sim 7.1$ ) film [21]. High dielectric constant of SBA compared to pure  $\text{Al}_2\text{O}_3$  is certainly due to incorporation of Na ions into  $\text{Al}_2\text{O}_3$  structure. However, the capacitance per unit area value ( $\sim 30 \text{ nF/cm}^2$  at 1 kHz) is lower than the value reported by Pal et al. ( $800 \text{ nF/cm}^2$  at 1 kHz; [3]). Moreover, the capacitance value of 2.1 nF at 1 kHz obtained in the present study is quite higher than the capacitance value reported by Lang et al. ( $\sim 22 \text{ pF}$  at 1 kHz)[4]. The difference in capacitance value in the present work compared to previous works, could be due to the different types of processing techniques employed to fabricate SBA film. Pal et al. fabricated SBA film using sol gel route while Lang et al. fabricated SBA film using reactive molecular beam epitaxial growth. In the present work, spray combustion synthesis technique was employed to fabricate SBA film. It is obvious that, films fabricated via different techniques will have different types of film morphology and will have different interfacial properties when in contact with other films. Liu et al. in their studies on SBA revealed that, the high capacitance value obtained in SBA based capacitors may be attributed to electric double layer capacitance (EDLC) formation, due to polarization of alkali ions at the SBA/ electrode interface [45]. Since interface of SBA/ electrode controls the EDLC formation, a future study could be dedicated to understand how the capacitance of SBA based capacitors changes when interface between SBA/electrode is altered.

Capacitance voltage measurement were also performed at 1 kHz operating frequency and is shown in Fig. 11(b), where we can observe that there is not much variation in capacitance over the entire voltage range from 3 V to -3 V. Good capacitance-voltage linearity is obtained here and such characteristic of dielectric is highly desirable when used as a gate dielectric in metal oxide semiconductor field effect transistors and passive component in analog and mixed signals (AMS) integrated circuits [46].

## Conclusion

Sodium  $\beta$ -alumina (SBA;  $\text{NaAl}_3\text{O}_7$ ) powder has been synthesized via versatile solution combustion technique using urea, glycine and citric acid. Among the three fuels used, urea showed highest combustion temperature (259 °C) and highest heat energy evolved (1452.4 J/g), whereas, citric acid showed the lowest combustion temperature (169 °C) as well as least evolved heat (161.9 J/g). Hence, crystalline SBA powder could be produced using urea in the as-combusted state itself without further calcination. On the other hand, powders produced from glycine and citric acid, were initially of amorphous nature, which might be due to lower exothermicity of the fuels and started to form  $m\text{-Al}_2\text{O}_3$  when calcined. From the thermodynamic and spectroscopic analyses it was observed that the exothermicity of different fuels used in the combustion reaction, mainly depends on the standard heat of formation of fuels and the complexation offered by the fuels to the metal cations. From the morphological analyses a very interesting fact was noticed, which showed that different morphologies of powders could be produced using different fuels and calcination treatment. SBA film fabricated using urea yielded crystalline SBA phase at 600 °C. Presence of Na, Al and O in the SBA film was confirmed using XPS and the film fabricated at 600 °C showed a high dielectric value ( $\epsilon_r$ ) of 21 at 1 kHz.

## Acknowledgement

This work is supported by Science and Engineering Research Board (SERB), Department of Science and Technology (ECR/2015/000339). The authors would like to thank Department of Metallurgical and Materials Engineering, NITK Surathkal, Department of Metallurgical and Materials Engineering (MEMS), IIT Bombay and Centre for Excellence in Nanotechnology (CEN), IIT Bombay for providing various facilities. The author would like to thank Dr. Praveen C. Ramamurthy (Associate Professor, IISc) for providing the lab facilities. Authors also extend regards to Dr. Srinivas Gandla, Mr. Sunil Meti, Mr. Dhanush and Ms. Rashmi for their timely assistance in Capacitor characterization, DSC, TEM and SEM respectively.

## References:

- [1] J. Walker, C. Catlow, The structure and energetics of the conduction plane in Na $\beta$  Al<sub>2</sub>O<sub>3</sub>, Nature 286 (1980) 473-474.
- [2] M.S. Whittingham, R.A. Huggins, Measurement of sodium ion transport in beta alumina using reversible solid electrodes, J. Chem. Phys. 54 (1971) 414-416.
- [3] B.N. Pal, B.M. Dhar, K.C. See, H.E. Katz, Solution-deposited sodium beta-alumina gate dielectrics for low-voltage and transparent field-effect transistors, Nat. Mater. 8 (2009) 898-903.
- [4] T. Ben-Lang, C. Chao, Z. Ji-Hua, Z. Wan-Li, L. Xing-Zhao, AlGaIn/GaN MISHEMTs with Sodium-Beta-Alumina as the Gate Dielectrics, Chin. Phys. Lett. 30 (2013) 026101.

- [5] G. Chen, J. Lu, X. Zhou, L. Chen, X. Jiang, Solid-state synthesis of high performance Na- $\beta$ '- $\text{Al}_2\text{O}_3$  solid electrolyte doped with MgO, *Ceram. Int.* 42 (2016) 16055-16062.
- [6] H.C. Park, Y.B. Lee, S.G. Lee, C.H. Lee, J.K. Kim, S.S. Hong, S.S. Park, Synthesis of beta-alumina powders by microwave heating from solution-derived precipitates, *Ceram. Int.* 31 (2005) 293-296.
- [7] D. Green, S. hutchison, Sintering sodium beta-alumina derived from solution spray-dried powders, *J. Can. Ceram. Soc.* 49, 1, 1980, (1980).
- [8] K. Kuribayashi, P.S. Nicholson, Dense conductive  $\beta$ '- $\text{Al}_2\text{O}_3$  ceramics by spray-freeze/freeze-drying, *Mater. Res. Bull.* 15 (1980) 1595-1601.
- [9] T. Girija, A.V. Virkar, Low temperature electrochemical cells with sodium  $\beta$ '-alumina solid electrolyte (BASE), *J. Power Sources* 180 (2008) 653-656.
- [10] X.-l. Wei, Y. Xia, X.-M. Liu, H. Yang, X.-D. Shen, Preparation of sodium beta'-alumina electrolyte thin film by electrophoretic deposition using Taguchi experimental design approach, *Electrochim. Acta* 136 (2014) 250-256.
- [11] T. Ben-Lang, C. Chao, L. Yan-Rong, Z. Wan-Li, L. Xing-Zhao, Sodium beta-alumina thin films as gate dielectrics for AlGaN/GaN metal—insulator—semiconductor high-electron-mobility transistors, *Chin. Phys. B.* 21 (2012) 126102.
- [12] C. Chi, H. Katsui, T. Goto, Preparation of Na- $\beta$ -alumina films by laser chemical vapor deposition, *Surf. Coat. Technol.* 276 (2015) 534-538.
- [13] K. Zhao, Y. Liu, S. Zeng, J. Yang, Y. Liu, Z. Zhan, L. Song, Preparation and characterization of a  $\text{ZrO}_2$ - $\text{TiO}_2$ -co-doped Na- $\beta$ '- $\text{Al}_2\text{O}_3$  ceramic thin film, *Ceram. Int.* 42 (2016) 8990-8996.

- [14] E. Caudron, G. Baud, J. Besse, M. Jacquet, G. Blondiaux, Elaboration and optimization of amorphous Na-Al-O thin films, *Solid State Ionics* 57 (1992) 189-192.
- [15] R. Vries, W. Roth, Critical Evaluation of the Literature Data on Beta Alumina and Related Phases: I, Phase Equilibria and Characterization of Beta Alumina Phases, *J. Am. Ceram. Soc.* 52 (1969) 364-369.
- [16] K.C. Patil, S.T. Aruna, T. Mimani, Combustion synthesis: an update, *Curr. Opin. Solid State Mater. Sci.* 6 (2002) 507-512.
- [17] M.-G. Kim, M.G. Kanatzidis, A. Facchetti, T.J. Marks, Low-temperature fabrication of high-performance metal oxide thin-film electronics via combustion processing, *Nat. Mater.* 10 (2011) 382-388.
- [18] J.-S. Seo, J.-H. Jeon, Y.H. Hwang, H. Park, M. Ryu, S.-H.K. Park, B.-S. Bae, Solution-processed flexible fluorine-doped indium zinc oxide thin-film transistors fabricated on plastic film at low temperature, *Sci. Rep.* 3 (2013) 2085.
- [19] B. Wang, X. Yu, P. Guo, W. Huang, L. Zeng, N. Zhou, L. Chi, M.J. Bedzyk, R.P. Chang, T.J. Marks, Solution-Processed All-Oxide Transparent High-Performance Transistors Fabricated by Spray-Combustion Synthesis, *Adv. Electron. Mater.* 2 (2016) 1-9.
- [20] A. Mali, A. Petric, Synthesis of sodium  $\beta''$ -alumina powder by sol-gel combustion, *J. Eur. Ceram. Soc.* 32 (2012) 1229-1234.
- [21] R. Branquinho, D. Salgueiro, L. Santos, P. Barquinha, L. Pereira, R. Martins, E. Fortunato, Aqueous combustion synthesis of aluminum oxide thin films and application as gate dielectric in GZTO solution-based TFTs, *ACS Appl. Mater. Interfaces* 6 (2014) 19592-19599.
- [22] V. Chandramouli, S. Anthonysamy, P.V. Rao, Combustion synthesis of thoria—a feasibility study, *J. Nucl. Mater.* 265 (1999) 255-261.

- [23] A. Varma, A.S. Mukasyan, A.S. Rogachev, K.V. Manukyan, Solution Combustion Synthesis of Nanoscale Materials, *Chem. Rev.* 116 (2016) 14493-14586.
- [24] F. Deganello, G. Marci, G. Deganello, Citrate–nitrate auto-combustion synthesis of perovskite-type nanopowders: a systematic approach, *J. Eur. Ceram. Soc.* 29 (2009) 439-450.
- [25] L.A. Chick, L. Pederson, G. Maupin, J. Bates, L. Thomas, G. Exarhos, Glycine-nitrate combustion synthesis of oxide ceramic powders, *Mater. Lett.* 10 (1990) 6-12.
- [26] P.M. Schaber, J. Colson, S. Higgins, D. Thielen, B. Anspach, J. Brauer, Thermal decomposition (pyrolysis) of urea in an open reaction vessel, *Thermochim. Acta* 424 (2004) 131-142.
- [27] K.V. Manukyan, A. Cross, S. Roslyakov, S. Rouvimov, A.S. Rogachev, E.E. Wolf, A.S. Mukasyan, Solution combustion synthesis of nano-crystalline metallic materials: mechanistic studies, *J. Phys. Chem. C* 117 (2013) 24417-24427.
- [28] M.M. Barbooti, D.A. Al-Sammerrai, Thermal decomposition of citric acid, *Thermochim. Acta*, 98 (1986) 119-126.
- [29] X. Lu, G. Xia, J.P. Lemmon, Z. Yang, Advanced materials for sodium-beta alumina batteries: status, challenges and perspectives, *J. Power Sources* 195 (2010) 2431-2442.
- [30] V. Jayaraman, G. Periaswami, T. Kutty, Extended stability ranges of  $\beta$ -aluminas with increasing ionic radii of metal alkali ions, *Mater. Lett.* 45 (2000) 71-78.
- [31] R. Subasri, S. Roy, D. Matusch, H. Näfe, F. Aldinger, Synthesis and Structural Characterization of a Metastable Mullite- Like Alumina Phase, *J. Am. Ceram. Soc.* 88 (2005) 1740-1746.
- [32] J.D. Hodge, powder processing and crystallization of  $\beta$  and  $\beta''$  aluminas, *Am. Ceram. Soc. Bull.* 62 (1983) 244.

- [33] L.S. Cividanes, T.M. Campos, L.A. Rodrigues, D.D. Brunelli, G.P. Thim, Review of mullite synthesis routes by sol-gel method, *J. Sol-Gel Sci. Technol.* 55 (2010) 111-125.
- [34] T. Takahashi, K. Kuwabara,  $\beta$ -Al<sub>2</sub>O<sub>3</sub> synthesis from m-Al<sub>2</sub>O<sub>3</sub>, *J. Appl. Electrochem.* 10 (1980) 291-297.
- [35] S. Yamaguchi, K. Terabe, Y. Iguchi, A. Imai, Formation and crystallization of beta-alumina from precursor prepared by sol-gel method using metal alkoxides, *Solid State Ionics* 25 (1987) 171-176.
- [36] P.E. Morgan, Low temperature synthetic studies of beta-aluminas, *Mater. Res. Bull.* 11 (1976) 233-241.
- [37] F. Li, K. Hu, J. Li, D. Zhang, G. Chen, Combustion synthesis of  $\gamma$ -lithium aluminate by using various fuels, *J. Nucl. Mater.* 300 (2002) 82-88.
- [38] H. Katsuki, A. Kawahara, S. Ohtsuki, Surface modification of alumina ceramics with needle-like mullite, *J. Mater. Sci. Lett.* 9 (1990) 1156-1158.
- [39] C. Sadik, I.-E. El Amrani, A. Albizane, Recent advances in silica-alumina refractory: A review, *J. Asian Ceram. Soc.* 2 (2014) 83-96.
- [40] W. Li, M. Anderson, K. Lu, J.Y. Walz, Fabrication of porous mullite by freeze casting and sintering of alumina-silica nanoparticles, *Adv. Syn. Proc. App. Nanostruct.: Ceramic. Trans.* 238 (2012) 57-64.
- [41] R.D.M. Soares, A.C.S. Sabioni, I.S. Resck, V.A.S. Falcomer, J.A. Dias, N.M.D. Silva, S.M.C.D. Menezes, G.M.D. Costa, Structural characterization of mullites synthesized by thermal decomposition of topaz, *Mat. Res.* 10 (2007) 75-78.

- [42] B. Zhang, Y. Liu, S. Agarwal, M.-L. Yeh, H.E. Katz, Structure, sodium ion role, and practical issues for  $\beta$ -alumina as a high-k solution-processed gate layer for transparent and low-voltage electronics, *ACS Appl. Mater. Interfaces* 3 (2011) 4254-4261.
- [43] J.W. Hennek, J. Smith, A. Yan, M.-G. Kim, W. Zhao, V.P. Dravid, A. Facchetti, T.J. Marks, Oxygen “getter” effects on microstructure and carrier transport in low temperature combustion-processed a-InXZnO (X= Ga, Sc, Y, La) transistors, *J. Am. Chem. Soc.* 135 (2013) 10729-10741.
- [44] A. Liu, G.X. Liu, H.H. Zhu, F. Xu, E. Fortunato, R. Martins, F.K. Shan, Fully Solution-Processed Low-Voltage Aqueous In<sub>2</sub>O<sub>3</sub> Thin-Film Transistors Using an Ultrathin ZrO<sub>x</sub> Dielectric, *ACS Appl. Mater. Interfaces* 6 (2014) 17364-17369.
- [45] Y. Liu, P. Guan, B. Zhang, M.L. Falk, H.E. Katz, Ion dependence of gate dielectric behavior of alkali metal ion-incorporated aluminas in oxide field-effect transistors, *Chem. Mater.* 25 (2013) 3788-3796.
- [46] M.-T. Yu, K.-Y. Chen, Y.-H. Chen, C.-C. Lin, Y.-H. Wu, TiO<sub>2</sub>-based MIM capacitors featuring suppressed leakage current by embedding Ge nanocrystals, *RSC Adv.* 5 (2015) 13550-13554.

**List of Figures**

Fig. 1. TGA traces of dried gel of (a) F<sub>1</sub>, (b) F<sub>2</sub> and (c) F<sub>3</sub>. Inset shows the color of powder after each stage of mass loss.

Fig. 2. DSC traces of dried gel of (a) F<sub>1</sub>, (b) F<sub>2</sub>, (c) F<sub>3</sub> and (d) plot of Al<sup>3+</sup> ion concentration (measured from ICP-OES study) in different fuel (red) and standard heat of formation of each fuel (blue). Inset in (d) shows the plot of enthalpy of combustion in each system.

Fig. 3. XRD peaks at different temperature of (a) F<sub>1</sub>, (b) F<sub>2</sub>, (c) F<sub>3</sub> and (d) crystallite size of powders of F<sub>1</sub>, F<sub>2</sub> and F<sub>3</sub> as a function of calcination temperature. Inset in (b) and (c) is the enlarged peak centered around  $2\theta = 26^\circ$ .

Fig. 4. SEM micrographs of powders obtained from F<sub>1</sub>: (a, b) as combusted powder, (c) EDS analysis of as combusted powder and (d) powder calcined at 900 °C.

Fig. 5. SEM micrographs of powders obtained from F<sub>2</sub>: (a) AC powder, (b) and (c) powder calcined at 900 °C.

Fig. 6. SEM micrographs of powders obtained from F<sub>3</sub>: (a) as combusted powder and (b) powder calcined at 900 °C.

Fig. 7. TEM micrographs of AC powders produced from F<sub>1</sub> at different magnification.

Fig. 8. GIAXRD pattern of SBA films using F<sub>1</sub>, fabricated at 300 °C and 600 °C.

Fig. 9. O1s spectra of SBA thin films fabricated at (a) 300 °C (b) 600 °C, (c) Na1s spectra of SBA films and (d) Al2p spectra of SBA films. Inset in (a) and (b) shows the concentration of various chemical binding states in oxygen atom.

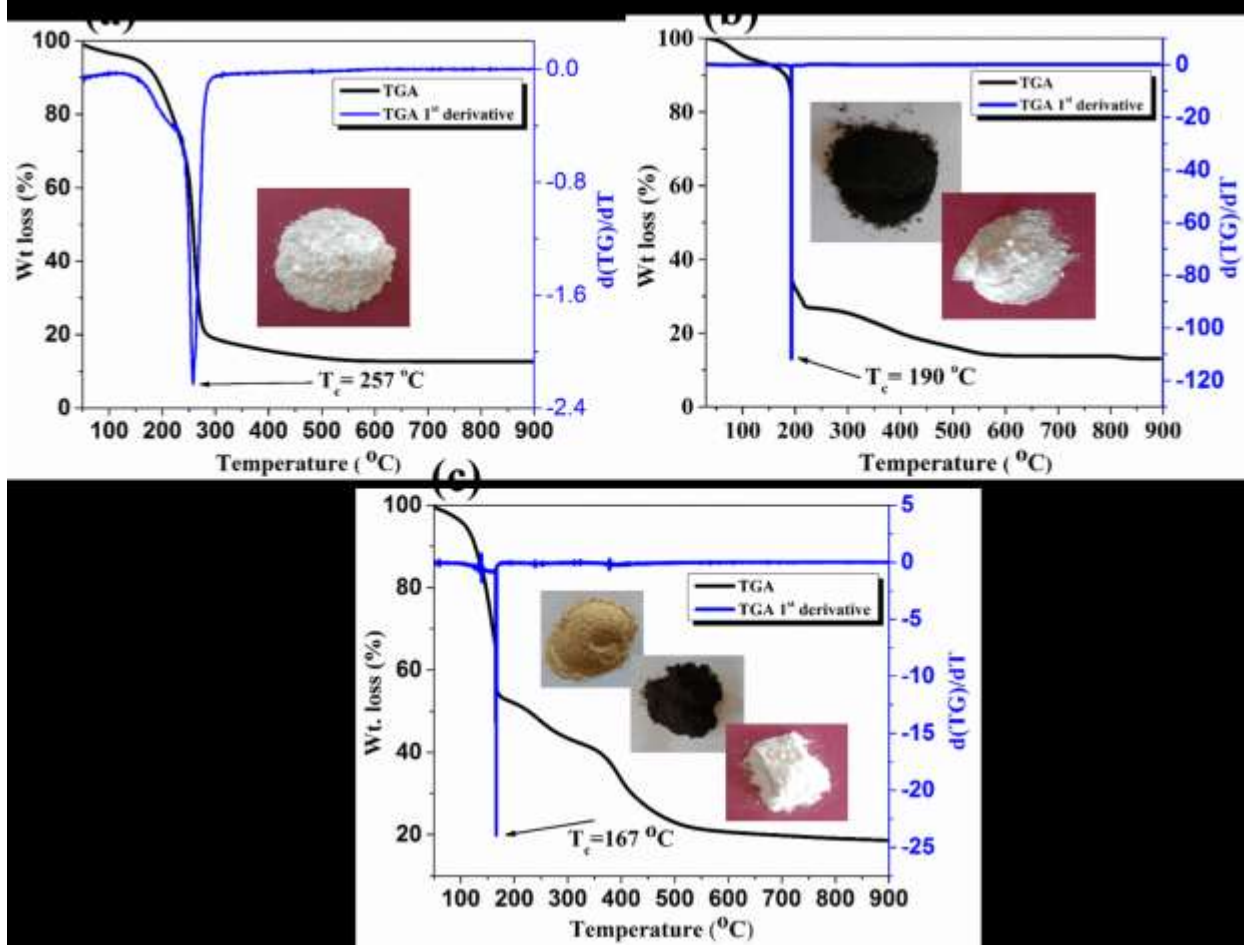
Fig.10. (a) Fabricated Au/SBA/Au MIM structure capacitor and (b) schematic of Au/SBA/ITO MIM structure capacitor.

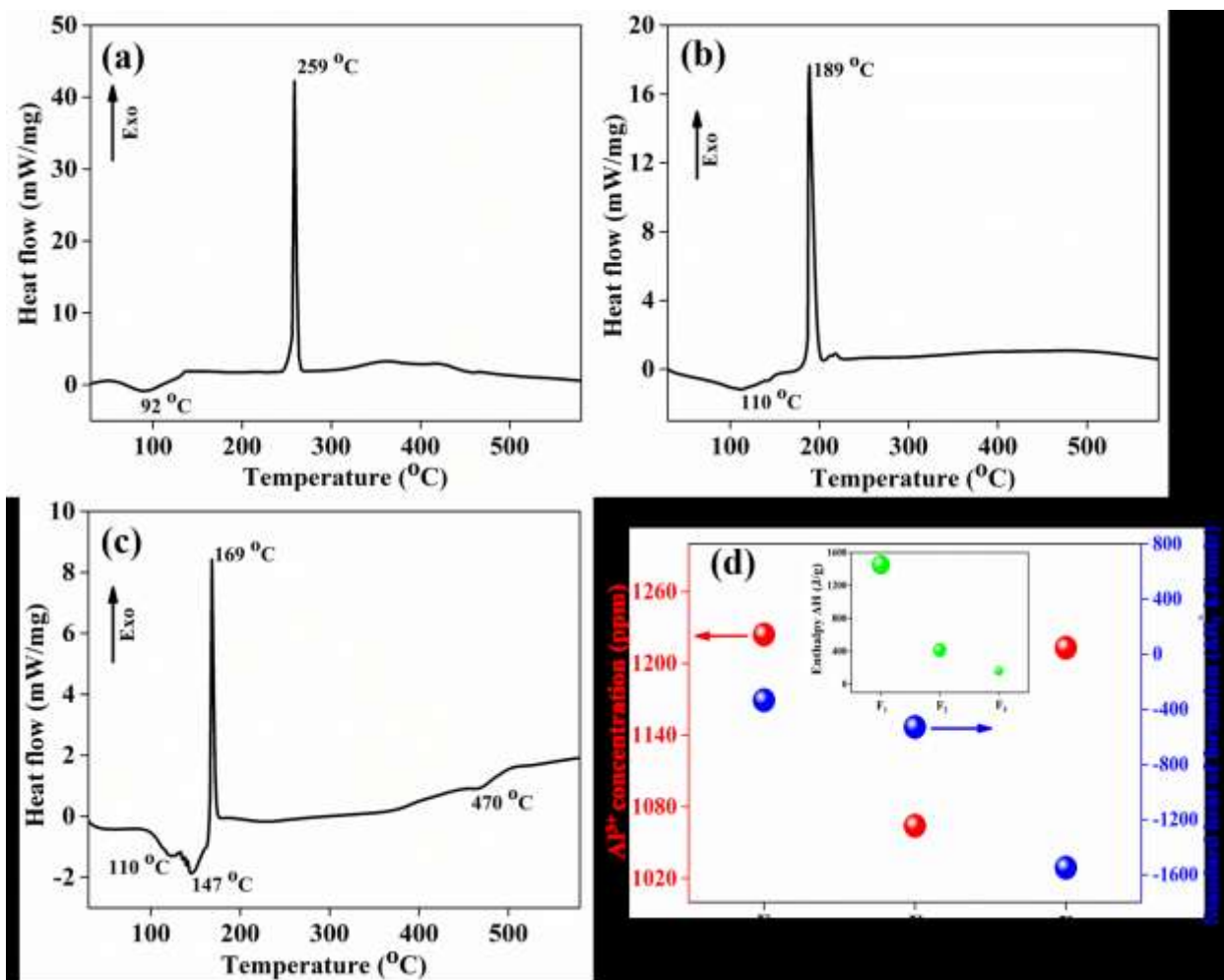
Fig. 11. Plot of capacitance as a function of (a) frequency and (b) voltage of Au/SBA/ITO MIM structure.

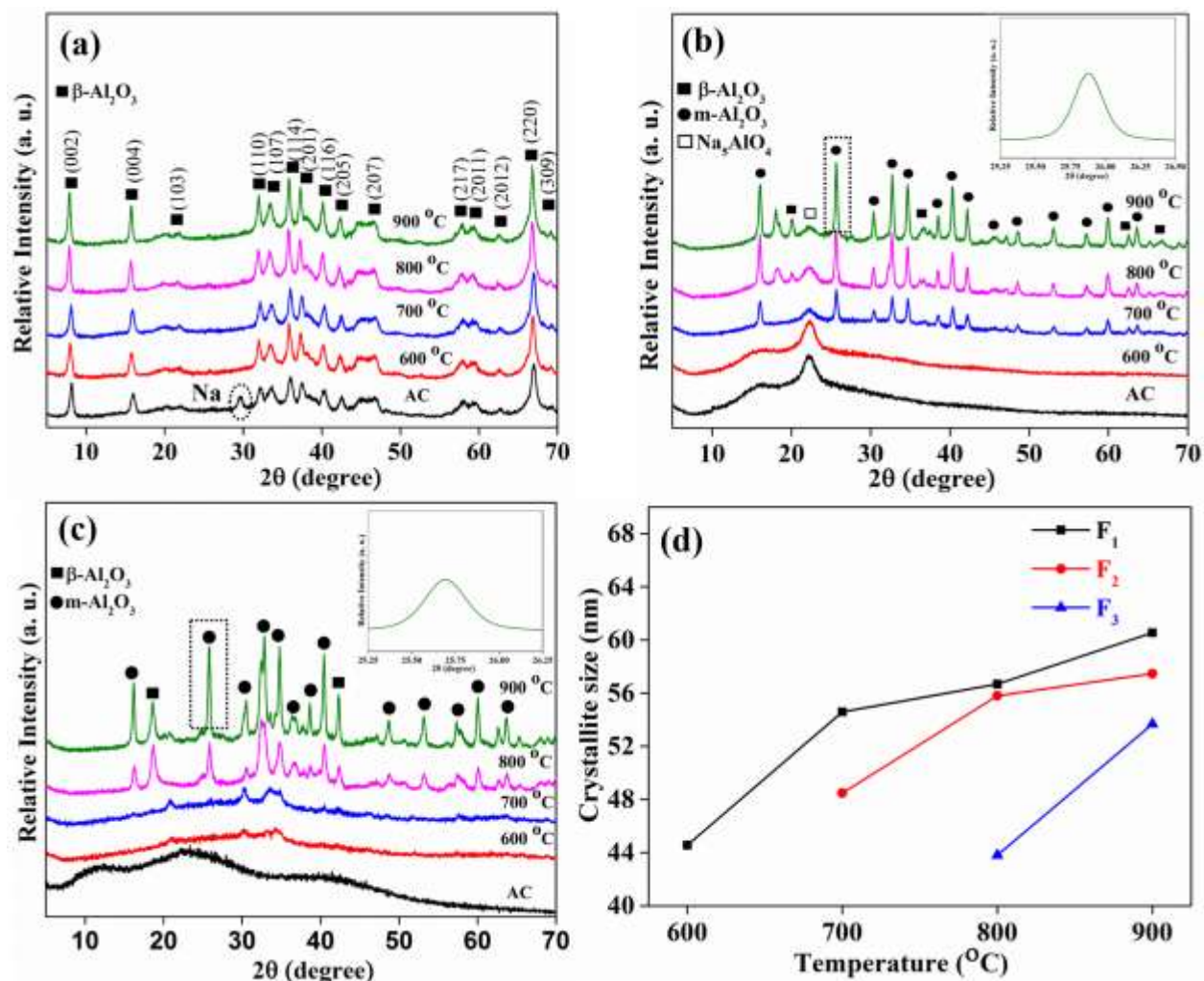
Accepted manuscript

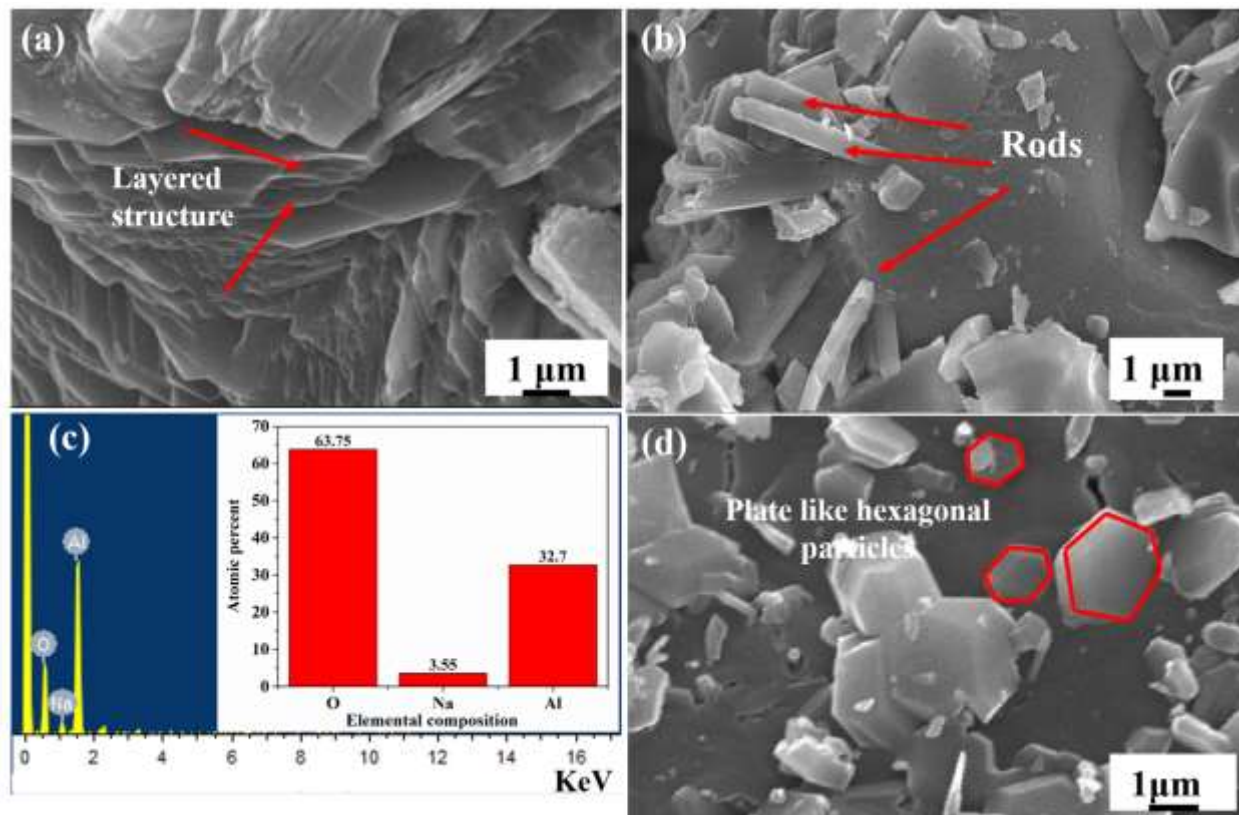
Table 1. Description of type of fuel, decomposition temperature of fuel, standard heat of formation of fuel, enthalpy of combustion, color of as combusted powder, combustion temperature, nature of combustion, moles of gases evolved.

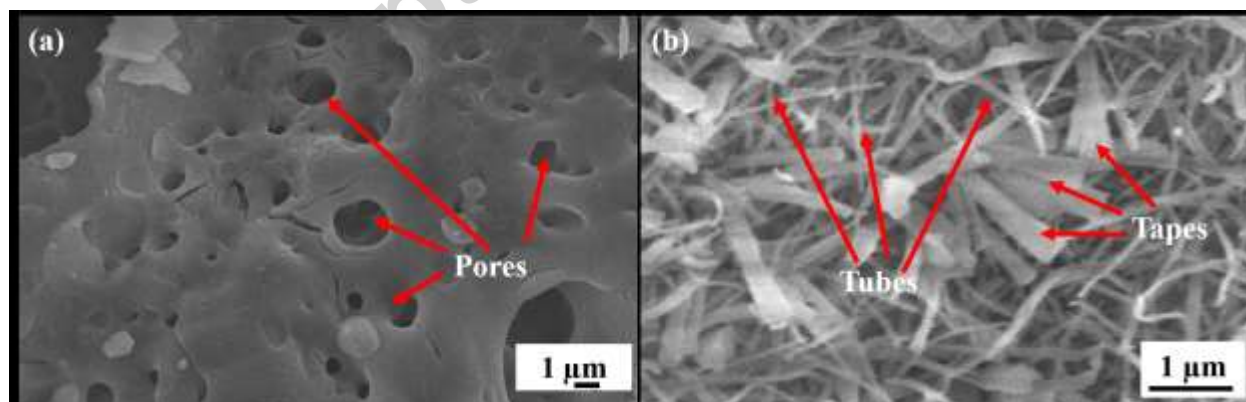
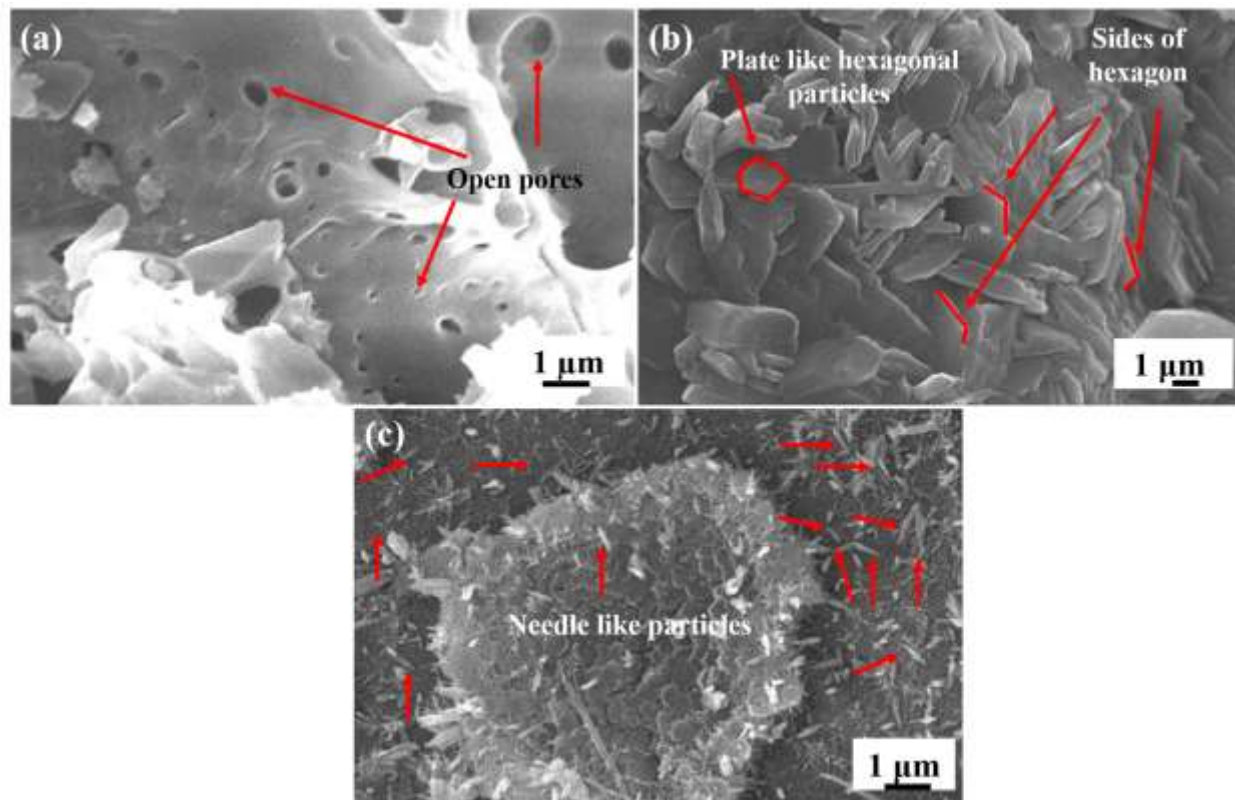
Sl. No.	Fuel	Decomposition Temperature of fuel	Standard heat of formation of each fuel $\Delta H_f^\circ$ (kJ/mole) [23]	Combustion temperature ( $T_c$ )	$\Delta H$ (J/g) of combustion (Calculated from DSC)	Color of as-combusted powder	Nature of combustion	Moles of gases evolved per mole of SBA (from balanced equation (1)-(3))
1.	Urea	Starts at 250 °C [26]	-333.5	259 °C	1452.4	White	Flaming	130.3
2.	Glycine	Starts at 180 °C [27]	-528.5	189 °C	415.7	Black	Smoldering	111.4
3.	Citric acid	Starts at 148 °C but rapids at 165 °C [28]	-1543.8	169 °C	161.9	Brown	Smoldering	111.4

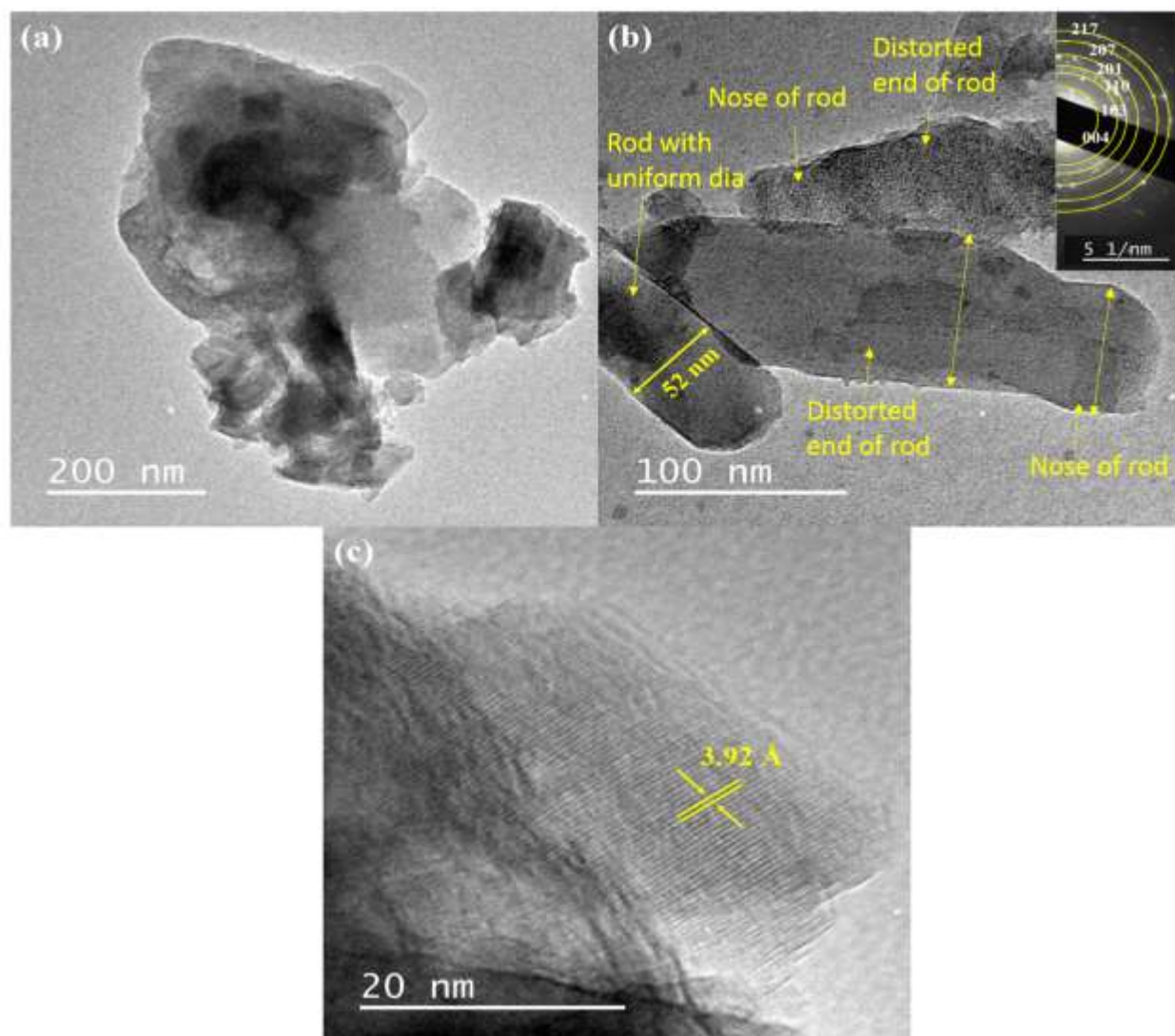


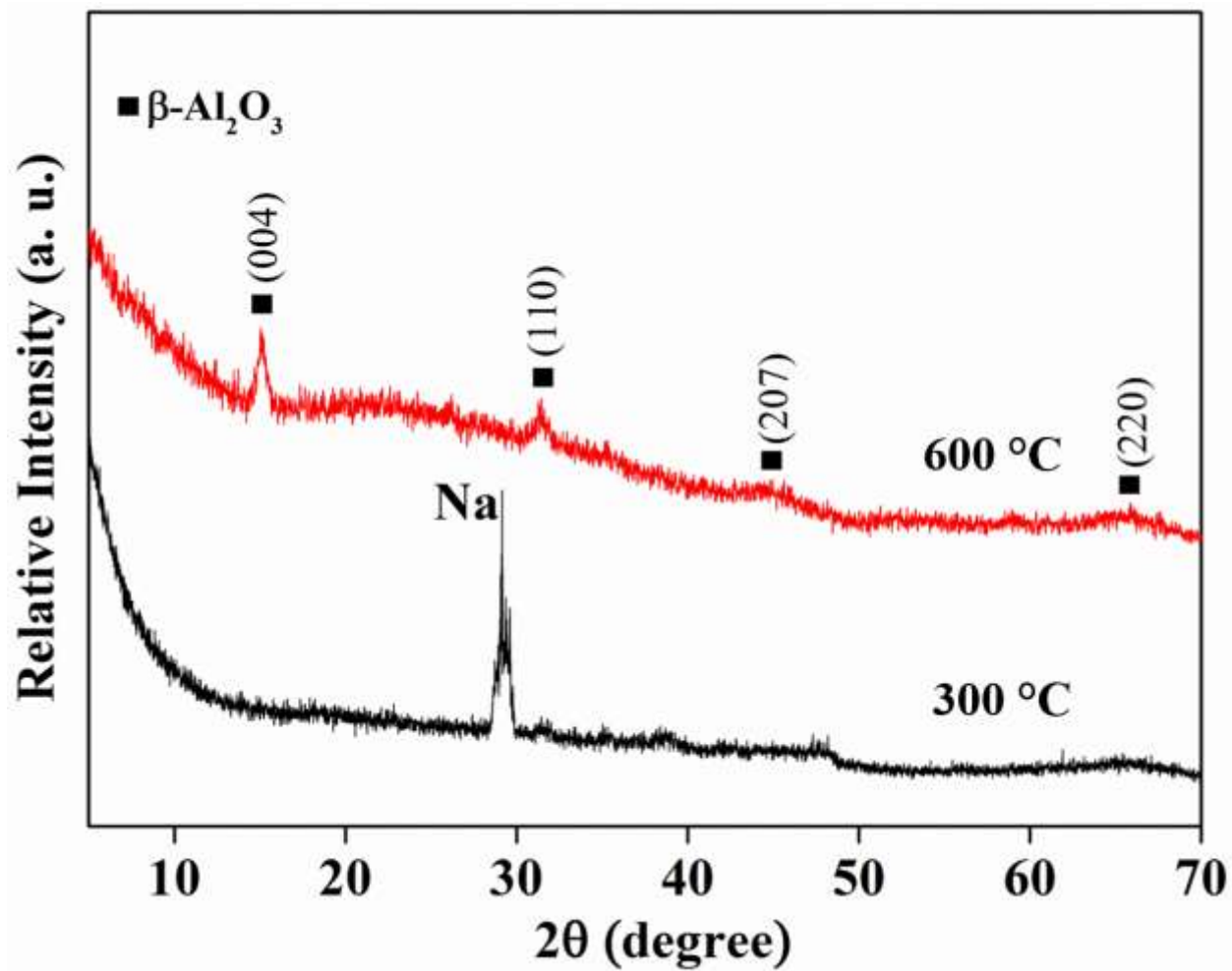




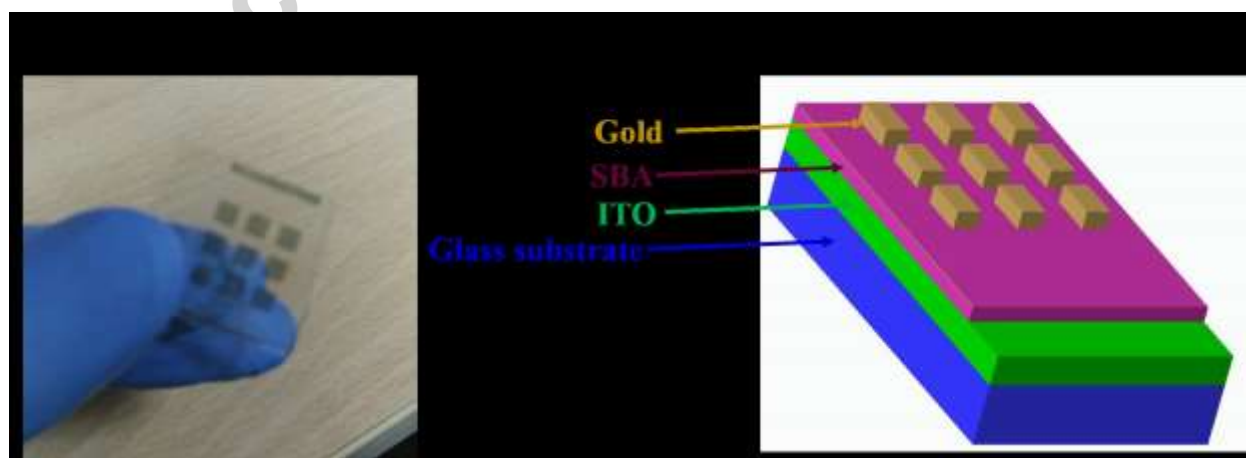
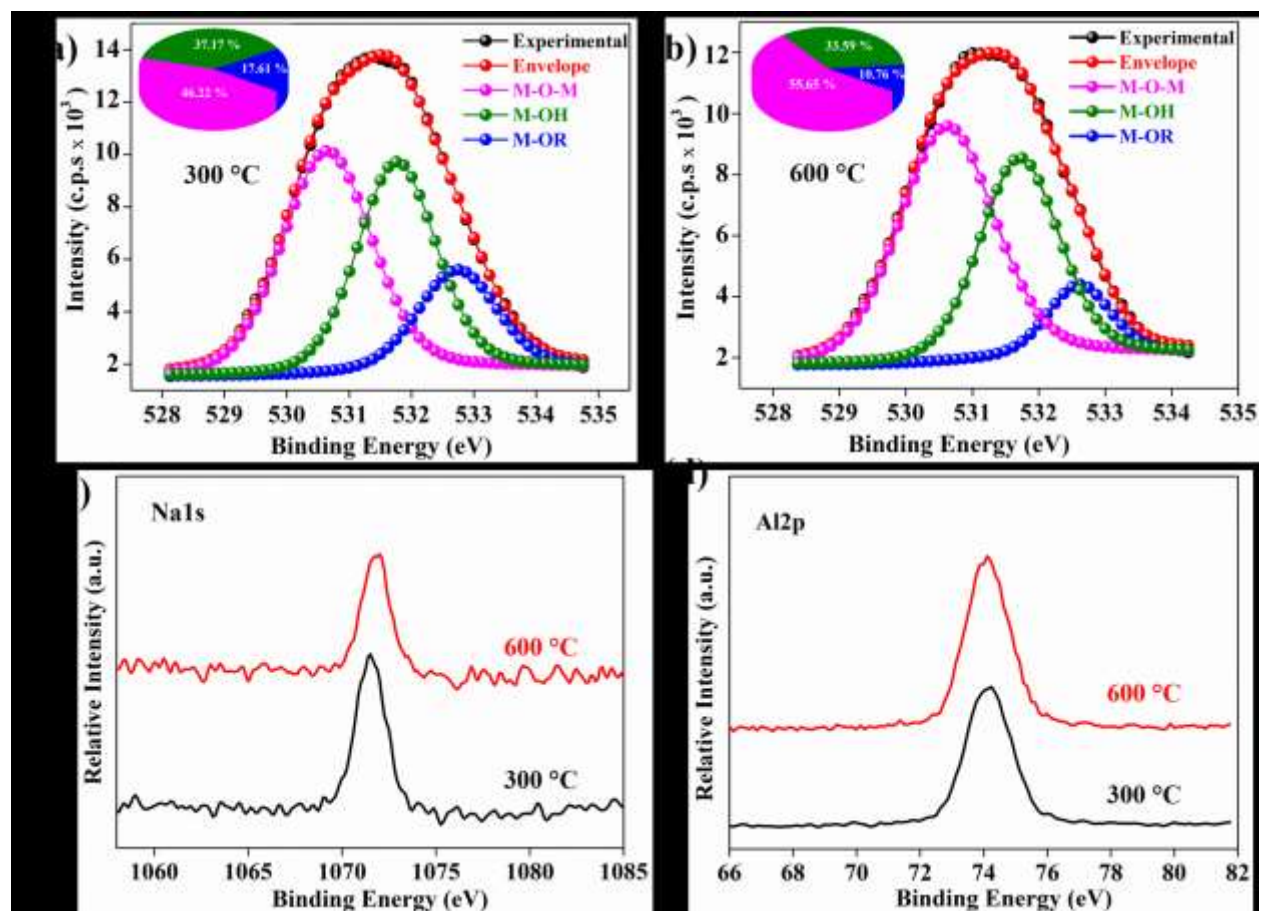


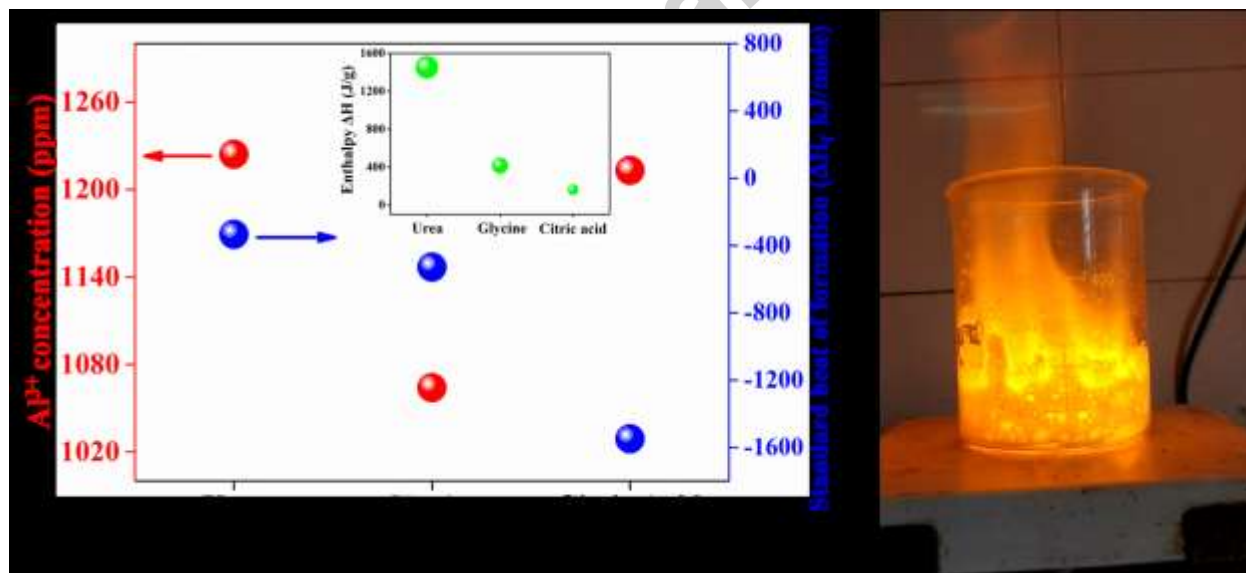
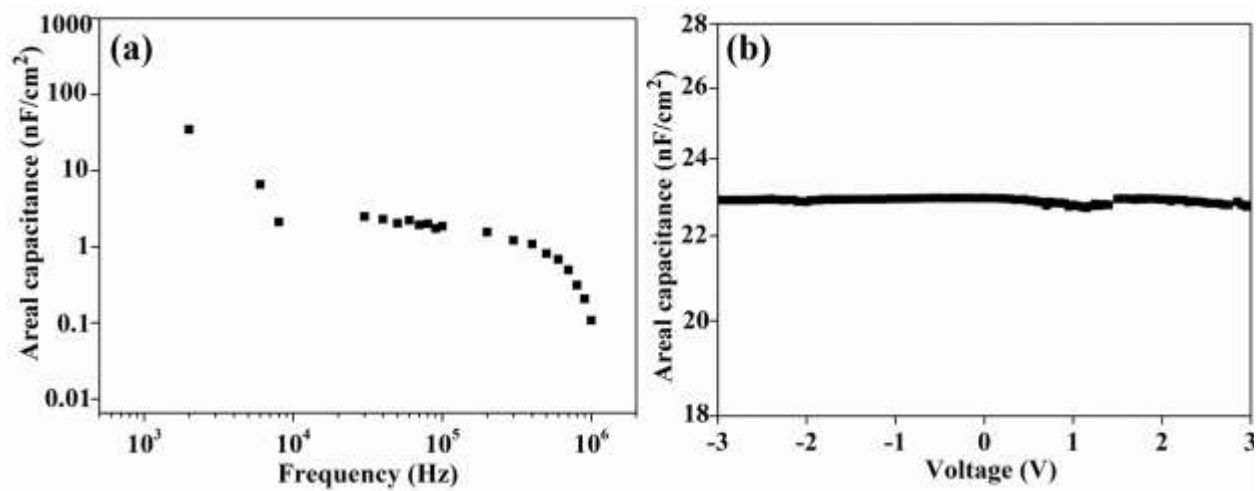






Accepted





Graphical abstract